

Jahn-Teller and related effects in the silver trimer. I. The *ab initio* calculation of spectroscopically observable parameters for the \tilde{X}^2E' and \tilde{A}^2E' electronic states

Ilias Sioutis, Vadim L. Stakhursky, Russell M. Pitzer, and Terry A. Miller

Department of Chemistry, The Ohio State University, 120 West 18th Avenue, Columbus, Ohio 43210

(Received 12 September 2006; accepted 7 December 2006; published online 26 March 2007)

Extensive *ab initio* calculations were performed for the \tilde{X}^2E' and \tilde{A}^2E'' states of Ag_3 , using a newly constructed basis set for Ag. An important goal of these calculations is to guide the analysis of the experimentally observed $\tilde{A}^2E''-\tilde{X}^2E'$ electronic spectrum. Vibrational frequencies of Ag_3 for both the \tilde{X} and \tilde{A} states are reported. Spectroscopically obtainable parameters describing the Jahn-Teller effect are calculated for the \tilde{X} and \tilde{A} states. The magnitude of the spin-orbit effects for this relativistic system was also calculated for the \tilde{X}^2E' and \tilde{A}^2E'' states. Using all this information, the $\tilde{X}-\tilde{A}$ electronic spectrum is predicted for Ag_3 . Additionally, the geometries and symmetries of the global minima and saddle points as well as the barrier to pseudorotation around the moat of the potential energy surface are determined for both states. © 2007 American Institute of Physics.

[DOI: 10.1063/1.2430703]

I. INTRODUCTION

Metal clusters are of considerable interest due to their role as a bridge between the atomic and solid states. The stabilities of small clusters and the evolution of bulk properties from cluster properties are the subject of nanoscience. Small clusters play an important role in homogeneous and heterogeneous catalysis, solid-state physics, crystal growth, and surface science.¹

Silver is important in photographic and catalytic processes.^{1,2} There is also an intriguing contrast between the bonding in silver and that in copper and gold. Among the simplest metal clusters are the homonuclear coinage metal trimers (Cu_3 , Ag_3 , and Au_3). While their ground-state electronic structure essentially corresponds to three metal atoms each with a single s electron, the d orbitals also play a role, particularly in electron correlation. The orbitally degenerate $\tilde{X}^2E' D_{3h}$ state of Ag_3 can undergo Jahn-Teller distortion to 2A_1 and 2B_2 states in C_{2v} symmetry. The spin-orbit splitting may partially quench this distortion. Thus silver trimer is an interesting candidate for the study of the interplay of the Jahn-Teller and spin-orbit effects.

Silver clusters have been a favorite target of theoreticians for nearly 30 years. Their primary focus was to understand and predict the molecule's geometries and electronic structures. Ag_3 has received special attention. Ionization energies, electron affinities, vertical detachment energies, electronic transition energies, and ground-state geometries for Ag_3 have been studied by previous workers.¹ Previous theoretical work on Ag_3 has not produced, however, any conclusive information about the Jahn-Teller effects.^{3–5}

Ag_3 has also stimulated experimental² interest, and considerable research was conducted in parallel to the theoretical work. Although experimentally it is possible to directly in-

vestigate the Jahn-Teller conical intersection, very little experimental work concerned itself with answering this central question. The vibronic spectrum of Ag_3 in the range of 370–365 nm was first reported and interpreted by Cheng and Duncan.^{6,7} The spectrum was assigned as the $\tilde{A}^2E'' \leftarrow \tilde{X}^2E'$ transition. Ellis *et al.*⁸ studied the fluorescence excitation of the \tilde{A}^2E'' state. They recorded the laser-induced dispersed-fluorescence spectra of Ag_3 by pumping several vibronic bands of the excited state. One year later, the same vibronic spectrum was remeasured and analyzed by Wedum *et al.*³ These authors empirically fitted the lower vibronic levels of the excited state to a theoretical spectrum generated from an $E \otimes e$ vibronic coupling scheme using two different methods. These included either spin-orbit coupling and linear-only Jahn-Teller coupling or linear and quadratic Jahn-Teller coupling and no spin-orbit coupling. While the excited-state vibronic structure was relatively well understood, the corresponding information for the ground state was not. Wallimann *et al.*⁴ applied the one-color resonant two-photon ionization technique to measure the $\tilde{A}^2E'' \leftarrow \tilde{X}^2E'$ transition of Ag_3 . There was a Jahn-Teller analysis that included linear and quadratic terms along with the spin-orbit interaction term. The fitting of the excited-state levels was empirical and led to a set of spectral parameters quite different from the previous values.³ The spin-orbit coupling parameter for the \tilde{A} state was found to be one order of magnitude higher. The excited-state intensity pattern was best simulated using a set of ground-state spectral parameters which, however, were not equally good for the ground state. Raman spectroscopy of matrix-isolated, mass-selected Ag_3 was reported by Haslett *et al.*⁵ The spectrum displayed a rich vibronic structure. They derived a set of \tilde{X} -state spectral parameters similar to the previous values.³

It is difficult with experiment alone to provide a definite answer as to the nature of the Jahn-Teller distortion, that is, whether it is dynamic or static. A suitable theoretical model that characterizes the Jahn-Teller-distorted potential energy surface (PES) and is in agreement with the experimental observation needs to be constructed. A reliable theoretical model may be constructed by use of high-level *ab initio* calculations.

In the succeeding paper,⁹ hereafter called Part II, we report and analyze previously⁸ acquired spectral results for Ag_3 . The resolved emission spectra from different vibronic levels of the \tilde{A} state provide a detailed map of the \tilde{X} -state vibronic structure. These spectra have very complex vibronic structures, which require the aid of *ab initio* calculations for a proper interpretation. Previous calculations have neither reached a consensus on the nature of the Jahn-Teller distortion in Ag_3 , nor calculated many parameters useful for spectral analysis; therefore we have undertaken a new series of calculations for the molecule with the explicit goal of predicting molecular parameters contained in the spectral analysis. Past work^{10,11} has presented theoretical approaches which we have extended¹² here with the express purpose of deriving the necessary spectral parameters for the analysis of the experimental spectra of Jahn-Teller-active molecules in their triangular configuration. In this paper we apply these approaches for the previously observed, quite complicated spectra of Ag_3 .

Experimentally observed electronic spectra reveal not only Jahn-Teller-active vibrations but also other allowed transitions to totally symmetric fundamentals, overtones, and the like. The data in Part II include emission spectra from several different \tilde{A} -state vibronic levels. These complementary spectra help assign the \tilde{X} -state vibronic levels, but only if the \tilde{A} -state vibronic assignments are known. Therefore we have performed calculations that help assign the \tilde{A} -state levels, as well as those of the \tilde{X} state.

The remainder of this paper is arranged as follows. The Hamiltonian used to interpret the spectroscopic results is briefly reviewed. The molecular parameters contained therein are explicitly related to topographic features of the PES obtainable as cuts of C_{2v} symmetry from the *ab initio* calculations. Results from several calculations for the \tilde{A} and \tilde{X} states are given. The *ab initio* results are then used to predict specific molecular parameters relevant to the spectral analysis. Finally, the various computational results are discussed, particularly with respect to their accuracy and usefulness for the spectral analysis. Part II contains the complete analysis of the spectra, using these calculations as the foundation of the analysis.

II. THE SILVER TRIMER POTENTIAL ENERGY SURFACE AND JAHN-TELLER EFFECTS

A. General features

The Jahn-Teller theory predicts that the \tilde{X}^2E' and \tilde{A}^2E'' electronic states of Ag_3 (D_{3h} symmetry) will interact with the e' vibration (see Fig. 1), leading to an adiabatic PES (APES)

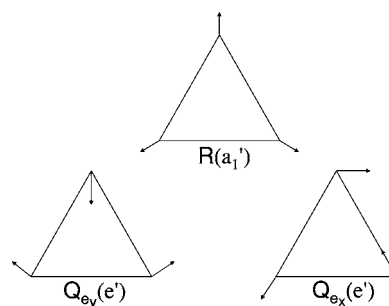


FIG. 1. The symmetry displacements of a planar triatomic equilateral nuclear conformation. The displacements Q_{e_y} and Q_{e_x} are, respectively, the real and imaginary parts of the complex coordinate $Q_{e',\pm}$.

with a circular trough (“Mexican hat”) when plotted versus the two coordinates of the degenerate mode. A reduction in symmetry to C_{2v} results in vibrations of symmetries a_1 and b_2 . As the molecule vibrates along the a_1 mode, the C_{2v} symmetry is retained, but for the b_2 mode it is not.

The lowest Jahn-Teller-split PES sheet is characterized by two sets of three equivalent extrema when the quadratic Jahn-Teller effect due to the e' mode is considered. These may be either global minima or saddle points. The degeneracy point represents a local cusplike maximum of the APES and is a conical intersection.

The spectroscopic problem at hand is to understand the observed structure in the $\tilde{A}^2E'' \leftarrow \tilde{X}^2E'$ electronic transition. This in turn corresponds to determining the positions of the vibronic levels within the \tilde{X} and \tilde{A} states. Consequently, any valid representation of the \tilde{A} - and \tilde{X} -state surfaces must yield a vibronic structure consistent with the experimental results.

The primary computational goal is to calculate the potential energy curves along the C_{2v} cuts through the e' vibrational subspace of the ground- and excited-Jahn-Teller-split C_{2v} electronic states. These cuts will lie along the a_1 component of the e' vibration, and they will also go through the potential minima of the lower APES of the \tilde{X}^2E' and \tilde{A}^2E'' states. The latter are expected to lie at opposite ends of the a_1 vibration and will correspond to C_{2v} triangular configurations with either elongated geometries or compressed ones along the in-plane z axis. The higher-energy potential minima correspond to the saddle points and the lower ones to the global minima, while their energy difference is the barrier to pseudorotation around the moat. Of equal interest is the energy of Ag_3 at the D_{3h} cusp, since it is with reference to this energy that the total (linear and quadratic) stabilization energy is measured.

In effect, the fundamental goals of this theoretical work are to try to determine for the \tilde{X}^2E' and \tilde{A}^2E'' states (1) the total Jahn-Teller stabilization (the energy difference between the conical intersection and the global minima); (2) the barrier to pseudorotation; (3) the geometries at the symmetric D_{3h} point, at the global minima, and at the saddle points, as well as the distances between them; and (4) the magnitude of the spin-orbit interaction.

B. Nuclear displacement coordinates

We start with an equilateral triangle geometry with its vertices labeled starting from 1 at the apex of the triangle and increasing in a clockwise manner to 2 and 3 at its base.

Following Ref. 10, the nuclear displacement coordinates may be expressed as

$$R[a_1] = \frac{1}{\sqrt{3}}(r_{12} + r_{13} + r_{23}), \quad (1)$$

$$Q_{e_x}[b_2] = \frac{1}{\sqrt{2}}(r_{12} - r_{13}), \quad (2)$$

$$Q_{e_y}[a_1] = \frac{1}{\sqrt{6}}(2r_{23} - r_{12} - r_{13}). \quad (3)$$

Their corresponding symmetries in the C_{2v} group are denoted in brackets. The nuclear displacement coordinate R describes the symmetric-stretch vibration, while Q_{e_x} and Q_{e_y} represent the bending mode with Q_{e_x} having asymmetric-stretch character at large displacements. Displacement in Q_{e_y} leads to either a narrow-angle (apex angle less than 60°) or a wide-angle (apex angle greater than 60°) isosceles triangle. Distortion along Q_{e_x} leads to a structure with C_s symmetry.

The distortion of Ag_3 along the e' Jahn-Teller coordinates may be conveniently visualized if we define polar coordinates ρ and ϕ to span the e' irreducible representation,

$$Q_{e_x} = \rho \cos \phi, \quad (4)$$

$$Q_{e_y} = \rho \sin \phi, \quad (5)$$

where $\rho = \sqrt{(Q_{e_x})^2 + (Q_{e_y})^2}$ and $\tan \phi = Q_{e_y}/Q_{e_x}$. The coordinates of the e' Jahn-Teller-active vibrational mode $Q_{e',\pm}$ may also be taken to be the complex combinations of the (Q_{e_x}, Q_{e_y}) coordinates,

$$Q_{e',\pm} = Q_{e_y} \pm iQ_{e_x} \quad (6)$$

(see also Fig. 1.)

C. The spectroscopic model of the Jahn-Teller PES

The Jahn-Teller effect may be described by Q_{e_x} and Q_{e_y} , two orthogonal vectors that span the space of the single e' molecular distortion. As they constitute a subspace of the $3N-6$ normal coordinate space (Q_i), the Jahn-Teller coordinates may be completely described in terms of linear combinations of the normal coordinates. It is hence convenient to work in the normal coordinate system of the undistorted symmetric molecule.

The general Hamiltonian for our system is

$$\hat{\mathcal{H}} = \hat{\mathcal{H}}_T + \hat{\mathcal{H}}_{SO} + \hat{\mathcal{H}}_e, \quad (7)$$

where $\hat{\mathcal{H}}_T$ is the nuclear kinetic energy, $\hat{\mathcal{H}}_{SO}$ is the spin-orbit coupling Hamiltonian, and $\hat{\mathcal{H}}_e$ is the electronic Hamiltonian. The spin-orbit coupling is expected to be nonzero for any open-shell orbitally degenerate electronic state. For Ag_3 the spin-orbit coupling is moderate for the \tilde{X}^2E' and \tilde{A}^2E''

TABLE I. The Jahn-Teller coupling coefficients that parametrize the effective spectroscopic Hamiltonian and their relationships to the terms of the Taylor series expansion of the potential.

Symbol	Description	Definition
$\lambda_{e'}$	Harmonic force constant of the Jahn-Teller-active e' mode	$\partial^2/(\partial Q_{e',+}\partial Q_{e',-})(\langle \Lambda_{\pm} \hat{\mathcal{H}}_e \Lambda_{\pm} \rangle)_0$
$\lambda_{a'_1}$	Harmonic force constant of the Jahn-Teller-inactive a'_1 mode	$\partial^2/\partial R^2(\langle \Lambda_{\pm} \hat{\mathcal{H}}_e \Lambda_{\pm} \rangle)_0$
$k_{e'}$	Linear Jahn-Teller coupling coefficient	$\partial/\partial Q_{e',\pm}(\langle \Lambda_{\pm} \hat{\mathcal{H}}_e \Lambda_{\mp} \rangle)_0$
$g_{e'}$	Quadratic Jahn-Teller coupling coefficient	$\partial^2/\partial Q_{e',\pm}^2(\langle \Lambda_{\pm} \hat{\mathcal{H}}_e \Lambda_{\mp} \rangle)_0$
$b_{a'_1 e'}$	Bilinear Jahn-Teller coupling coefficient	$\partial^2/\partial R \partial Q_{e',\pm}(\langle \Lambda_{\pm} \hat{\mathcal{H}}_e \Lambda_{\mp} \rangle)_0$

states, so $\hat{\mathcal{H}}_{SO}$ should not be discarded. We shall confine ourselves here to an analysis that initially omits the spin-orbit coupling and then we will address its effect as a second step in Sec. II E.

We consider the PES for a doubly degenerate electronic state of the nominally D_{3h} Ag_3 . In Ref. 13 we showed, as did others, that the PESs, V_{\pm} , of a Jahn-Teller-active molecule may be represented in terms of matrix elements of the electronic Hamiltonian $\hat{\mathcal{H}}_e$ i.e.,

$$V_{\pm} = \langle \Lambda_{+} | \hat{\mathcal{H}}_e | \Lambda_{+} \rangle \pm (\langle \Lambda_{+} | \hat{\mathcal{H}}_e | \Lambda_{-} \rangle \langle \Lambda_{-} | \hat{\mathcal{H}}_e | \Lambda_{+} \rangle)^{1/2}, \quad (8)$$

where $\langle \Lambda_{+} | \hat{\mathcal{H}}_e | \Lambda_{+} \rangle = \langle \Lambda_{-} | \hat{\mathcal{H}}_e | \Lambda_{-} \rangle$ and Λ_{\pm} are complex wave functions related to the real electronic wave functions, Λ_a and Λ_b by $\Lambda_{\pm} = (\Lambda_a \pm i\Lambda_b)/\sqrt{2}$. The diagonal and off-diagonal terms of Eq. (8) for Ag_3 may be written in a power series expansion,

$$\langle \Lambda_{+} | \hat{\mathcal{H}}_e | \Lambda_{+} \rangle = \sum_{r=+, -} \frac{1}{2} \lambda_{e'} |Q_{e',r}|^2 + \frac{1}{2} \lambda_{a'_1} |R|^2, \quad (9)$$

$$\langle \Lambda_{+} | \hat{\mathcal{H}}_e | \Lambda_{-} \rangle = k_{e'} Q_{e',+} + \frac{1}{2} g_{e'} (Q_{e',-})^2 + \frac{1}{2} b_{a'_1 e'} (Q_{e',+} R), \quad (10)$$

where, in Eqs. (9) and (10), the expansion has been truncated at second order, giving a parametrized spectroscopic potential. The parameters are the harmonic force constant of the e' or a'_1 mode represented, respectively, by $\lambda_{e'}$ and $\lambda_{a'_1}$; the linear Jahn-Teller coupling coefficient due to the Jahn-Teller-active e' mode, $k_{e'}$; the Jahn-Teller quadratic coupling coefficient $g_{e'}$; and the quadratic coupling coefficient between the e' coordinate and the a'_1 coordinate called¹⁴ the bilinear coupling coefficient $b_{a'_1 e'}$. These parameter definitions are summarized in Table I.

We mainly consider the linear Jahn-Teller term $k_{e'}$ and the quadratic Jahn-Teller term $g_{e'}$. The only remaining non-zero term is the bilinear term $b_{a'_1 e'}$, for which, although we have not rigorously calculated it, we have approximate estimates for the \tilde{X} and \tilde{A} states. It has previously been shown by Höper *et al.*¹⁵ that this term has little effect on the vibronic spectrum of CH_3O . Additionally, the experimental results for $\text{C}_5(\text{H/D})_5$ (Ref. 16) and for the closely related molecules $\text{C}_6(\text{H/F})_6^+$ and $\text{C}_6\text{H}_3\text{F}_3^+$ (Ref. 17) have been successfully ana-

lyzed without invoking this term. The primary goal of this work is to provide reasonable estimates of the most critical molecular parameters, which are the Jahn-Teller constants. These will be used to initiate the vibronic analysis of the experimental spectra of the \tilde{A}^2E'' and \tilde{X}^2E' states.

The topography of the PES is quite dependent on the symmetry of the normal coordinate along which one views the PES. The entire PES, neglecting the bilinear Jahn-Teller term, is defined by the following equation:

$$V_{\pm} = V_{\pm,e'}^{l,q} + V_{\pm,a'_1}^h, \quad (11)$$

where

$$\begin{aligned} V_{\pm,e'}^{l,q} &= \frac{1}{2}\lambda_{e'}\rho^2 \pm k_{e'}\rho \left(1 + \frac{2g_{e'}\rho}{k_{e'}} \cos(3\phi) + \frac{g_{e'}^2\rho^2}{k_{e'}^2} \right)^{1/2} \\ &\approx \frac{1}{2}\lambda_{e'}\rho^2 \pm [k_{e'}\rho + g_{e'}\rho^2 \cos(3\phi)], \end{aligned} \quad (12)$$

$$V_{\pm,a'_1}^h = \frac{1}{2}\lambda_{a'_1}R^2, \quad (13)$$

following the polar coordinate representation of the doubly degenerate normal coordinate. In the last equality of Eq. (12) the expansion of the radical has been truncated at the quadratic term in ρ . With the assumption that $k_{e'}$ and $g_{e'}$ are positive, the plus sign in the above equations corresponds to the upper sheet of the PES and the minus sign to the lower sheet. Then $V_{\pm,e'}^{l,q}$ adds the linear and quadratic Jahn-Teller term to the harmonic oscillator to describe the linear and quadratic Jahn-Teller PES seen along the e' normal coordinate. V_{\pm,a'_1}^h refers to the harmonic oscillator potential seen along the single Jahn-Teller-inactive normal coordinate.

We introduce the previously defined^{13,16} $\omega_{e,e'}$, the harmonic vibrational frequency of the e' mode evaluated at the conical intersection of the PES, $D_{e'}$, the linear Jahn-Teller coupling constant, and $K_{e'}$, the quadratic Jahn-Teller coupling constant, and we also define and use here the bilinear Jahn-Teller coupling constant $B_{a'_1 e'}$,

$$\omega_{e,e'} = \frac{1}{2\pi c} \left(\frac{\lambda_{e'}}{M_{e'}} \right)^{1/2}, \quad (14)$$

$$D_{e'} = \frac{k_{e'}^2}{2\hbar} \left(\frac{M_{e'}}{\lambda_{e'}^{1/3}} \right)^{1/2}, \quad (15)$$

$$K_{e'} = \frac{g_{e'}}{\lambda_{e'}}, \quad (16)$$

$$B_{a'_1 e'} = \frac{b_{a'_1 e'}}{\sqrt{\omega_{e,e'} \omega_{e,a'_1}}}, \quad (17)$$

where $M_{e'}$ corresponds to the reduced mass of the e' vibrational mode of Ag₃. If $g_{e'}$ is positive the minima about the moat will be at $\phi=0, 2\pi/3, 4\pi/3$ and the maxima will be at $\phi=\pi/3, \pi, 5\pi/3$. A negative value of $g_{e'}$ (relative to $k_{e'}$) generates a $\pi/3$ rotation in the e' vibrational space. This in turn leads to a reversal on the values of ϕ for the maxima

and minima. The following equations¹¹ result from taking the derivative of Eq. (12) with respect to ρ and setting it to zero with $\phi=0$ and $\pi/3$:

$$\rho_{e'}^0 = \frac{k_{e'}}{\lambda_{e'}(1-2K_{e'})} = \frac{1}{(1-2K_{e'})} \left(\frac{D_{e'}\hbar}{\pi c M_{e'} \omega_{e,e'}} \right)^{1/2}, \quad (18)$$

$$E_{e'}^0 = -\frac{k_{e'}^2}{2\lambda_{e'}(1-2K_{e'})} = -\frac{2\hbar\pi c D_{e'} \omega_{e,e'}}{(1-2K_{e'})}, \quad (19)$$

$$\rho_{e'}^{\pi/3} = \frac{k_{e'}}{\lambda_{e'}(1+2K_{e'})} = \frac{1}{(1+2K_{e'})} \left(\frac{D_{e'}\hbar}{\pi c M_{e'} \omega_{e,e'}} \right)^{1/2}, \quad (20)$$

$$E_{e'}^{\pi/3} = -\frac{k_{e'}^2}{2\lambda_{e'}(1+2K_{e'})} = -\frac{2\hbar\pi c D_{e'} \omega_{e,e'}}{(1+2K_{e'})}, \quad (21)$$

$$\Delta E_{e'}^B = |E_{e'}^0 - E_{e'}^{\pi/3}|, \quad (22)$$

where the superscripts 0 and $\pi/3$ indicate solutions at $\phi=0$ and $\phi=\pi/3$, respectively. The distance from the symmetric point to the distorted potential energy minima is given by $\rho_{e'}^0$ and $\rho_{e'}^{\pi/3}$. The total linear and quadratic Jahn-Teller stabilization energy is calculated for the angles that correspond to the global minima. The energies are given with respect to the conical intersection. The total Jahn-Teller stabilization energy is given, within this approximation, by $E_{e'}^0$ or $E_{e'}^{\pi/3}$ depending on whether $\phi=0$ or $\phi=\pi/3$ gives the largest energy. The barrier to pseudorotation around the moat is given by $\Delta E_{e'}^B$.

D. Relating the spectroscopic model to *ab initio* results

The slice along the Q_{e_y} coordinate of the PES represents a cross section that preserves the C_{2v} symmetry. It also includes the most important points of the PES: a global minimum, a saddle point, and the conical intersection. Additional information about the atomic displacements that one must apply to the symmetric configuration to reach the global minimum and saddle point may be extracted. These correspond to the distortion vectors ρ taken along the Q_{e_y} coordinate.

To further simplify Eqs. (12) for this cross section, we choose $\phi=0$. The addition and subtraction of the resulting equations lead to

$$V_+ + V_- \approx \lambda_{e'}\rho^2, \quad (23)$$

$$(V_+ - V_-)/2 \approx k_{e'}\rho + g_{e'}\rho^2, \quad (24)$$

where V_{\pm} is measured relative to the energy at the conical intersection and the distortion parameter ρ measures the atomic displacements from the same point. The barrier to pseudorotation around the moat, $\Delta E_{e'}^B$, may be obtained from

$$\begin{aligned}\Delta E_{e'}^B \approx & \frac{1}{2} \lambda_{e'} (\rho_{\max}^2 - \rho_{\min}^2) + k_{e'} (\rho_{\max} + \rho_{\min}) \\ & + g_{e'} (\rho_{\max}^2 + \rho_{\min}^2),\end{aligned}\quad (25)$$

where ρ_{\min} and ρ_{\max} point to the global minimum and local maximum of the Jahn-Teller-distorted PES. (Notice that in this formalism ρ_{\max} may be negative.)

Equations (23) and (24) will result in reliable estimates for $\lambda_{e'}$ and $k_{e'}$ based on a grid of PES points lying in the vicinity of the conical intersection. Equation (25) may be used for the calculation of the quadratic Jahn-Teller coefficient. It gives the barrier to pseudorotation from the energy difference between the extrema points of the Jahn-Teller-distorted PES. This energy difference is a known parameter from our *ab initio* calculations. It builds up mainly due to the quadratic Jahn-Teller effect. It makes use of directly available topographical characteristics of the PES such as ρ_{\min} and ρ_{\max} which can be calculated with greater reliability within our approach. Use of this equation avoids the inherently greater computational errors arising from using regions of the PES that are farther from the symmetric point; $g_{e'}$, as a quadratic constant, is normally smaller relative to $k_{e'}$ and is susceptible to greater error especially when it attains values that are at or near the limit of the reliability of the calculations. We place greater confidence in calculating the quadratic Jahn-Teller constant in this way. Also, by computing the ratio of Eqs. (19) and (21) we can calculate the value of its unitless expression, $K_{e'}$, i.e.,

$$\frac{E_{e'}^0}{E_{e'}^{\pi/3}} = \left(\frac{1 + 2K_{e'}}{1 - 2K_{e'}} \right). \quad (26)$$

An obvious last alternative would be to perform a direct evaluation of the constants using the definitions given in Table I. In principle this is possible with very high accuracy wave functions. However, one should not underestimate the difficulty of such calculations due to the wave-function error and therefore failure to obey the Hellmann-Feynman theorem.^{18,19}

We sampled points of D_{3h} symmetry. As the breathing mode of Ag_3 does not lower the symmetry of the molecule, the potential along the a'_1 vibration that crosses the conical intersection necessarily corresponds to a D_{3h} cut of the PES. The harmonic force constant of a'_1 at the conical intersection was calculated based on a quadratic fit and by using a grid of points lying in the vicinity of the conical intersection. To estimate $b_{a'_1 e'}$ in the \tilde{X} and \tilde{A} states, we computed the PES for a range of Q_{e_y} and R values.

With the theoretically calculated values of $\lambda_{a'_1}$, $\lambda_{e'}$, $k_{e'}$, and $b_{a'_1 e'}$ at hand we can easily calculate the harmonic frequencies of the a'_1 and e' modes based on Eq. (14) as well as the Jahn-Teller molecular parameters $D_{e'}$, $K_{e'}$, and $B_{a'_1 e'}$ using Eqs. (15)–(17). The frequencies of the a'_1 and e' modes at the stationary points were not given because they are not directly related to the analysis of the experimental spectra. While the harmonic frequency of the totally symmetric mode at the conical intersection could be useful in such analyses, the one due to the Jahn-Teller-active mode is of little direct

value owing to the convoluted topology of its vibronic space. The constants obtained in this manner were used in the spectroscopic analysis.

E. Adding the spin-orbit interaction to the spectroscopic model

Ag_3 is a heavy molecule and is hence subject to relativistic effects which makes $\hat{\mathcal{H}}_{\text{SO}}$ non-negligible. The spin-orbit coupling interaction partially quenches the Jahn-Teller effect (and vice versa), thus a suitable theoretical treatment is needed to account for it. Following the Barckholtz and Miller methodology,¹¹ the potentials in the presence of linear and quadratic Jahn-Teller effects and spin-orbit coupling for a degenerate mode, $V_{\pm, e'}^{l, q, \text{SO}}$, are given by

$$\begin{aligned}V_{\pm, e'}^{l, q, \text{SO}} = & \frac{1}{2} \lambda_{e'} \rho^2 \pm \frac{1}{2} [(\alpha \zeta_e)^2 + 4k_{e'}^2 \rho^2 \\ & + 8g_{e'} k_{e'} \rho^3 \cos(3\phi)]^{1/2}.\end{aligned}\quad (27)$$

It is apparent from the square root in this equation that the effect of the spin-orbit interaction is a maximum at $\rho=0$ and decreases rapidly as ρ increases. Due to the fact that the projection Σ of the electron spin S on the C_3 axis is still approximately preserved, the eigenvalues $V_{\pm, e'}^{l, q, \text{SO}}$ are each degenerate. The product $\alpha \zeta_e$ corresponds to a parametrized expression for the spin-orbit Hamiltonian $\hat{\mathcal{H}}_{\text{SO}}$, where ζ_e is the projection of the electronic orbital angular momentum on the principal axis and α is the spin-orbit coupling constant.¹¹

F. Relating the spin-orbit spectroscopic model to *ab initio* results

We outline here the approach that we follow to theoretically calculate the effect of the spin-orbit interaction in Ag_3 . It is effectively represented by the traditional spectroscopic spin-orbit coupling parameter $\alpha \zeta_e$. We discuss the relationship between the theoretically determined and spectroscopically approximated expressions for the spin-orbit interaction. The primary objective is to obtain a theoretically calculated estimate for the spin-orbit coupling that is also, in essence, compatible with the parametrized expression $\alpha \zeta_e$ and hence to make use of this in our spectroscopic model.

Once spin-orbit coupling is considered in the problem, the two surfaces of the Jahn-Teller-distorted PES no longer intersect at $\rho=0$; they become separated by an energy difference that depends directly on the magnitude of the spin-orbit coupling. The two curves present the characteristics of an avoided crossing. Assuming a moderate spin-orbit interaction in the presence of Jahn-Teller effects, one would anticipate the upper surface to exhibit a minimum at the symmetric configuration and the lower one to have a maximum at the same point of the PES.

The addition of Eq. (27), for $\phi=0$, gives

$$V_+ + V_- = \lambda_{e'} \rho^2, \quad (28)$$

while the subtraction of Eq. (27), for $\phi=0$ and $\rho=0$, gives

$$V_+ - V_- = \alpha \zeta_e. \quad (29)$$

Equation (28) shows that the e' harmonic force constant may be calculated in a way unaffected by the spin-orbit coupling.

Equation (29) shows that the energy difference between the Jahn-Teller-split potential energy curves due to the spin-orbit interaction is $\alpha\zeta_e$. The spin-orbit interaction that we report in Sec. IV for the \tilde{X}^2E' and \tilde{A}^2E'' states refers to $\alpha\zeta_e$. It will be used as an effective spin-orbit parameter in the calculation of the spin-vibronic levels in the \tilde{X}^2E' and \tilde{A}^2E'' states of Ag_3 in Part II.

The spin-orbit coupling in the valence shell of Ag_3 is addressed by the valence spin-orbit operators and was calculated by the COLUMBUS suite of programs.²⁰ The spin-orbit operators include the (large) spin-orbit interactions of the valence electrons with the nucleus and with the core electrons as well as an approximation to the (small) spin-orbit interaction between the valence electrons. To include or omit the spin-orbit operators in the calculation is an option in COLUMBUS. To estimate the spin-orbit effects of Ag_3 one simply needs to carry out the calculation twice, i.e., in the absence and in the presence of the spin-orbit operators. Once they have been included, the calculation may be carried out in a single step, with no implicit or explicit assumptions about the size of the spin-orbit interaction compared to the other interactions, and within a larger configuration space.

III. COMPUTATIONAL DETAILS

A. Electronic structure calculations

All of the computations were carried out with relativistic effective core potentials (RECPs) that retained the outer $4s^24p^64d^{10}5s^1$ shells of the Ag atoms in the valence space, replacing the remaining 28 electrons by RECPs. Hence 57 electrons were explicitly treated in the calculations for Ag_3 . The RECPs and spin-orbit operators were taken from the work of Christiansen *et al.*²¹ We used our newly developed basis set of Ag which corresponds to a generally contracted valence Gaussian basis set (see Sec. III B). The number of spin eigenfunctions [configuration state functions, (CSFs)] in the wave-function expansions varied from 3.9×10^6 to 48×10^6 , with the larger values occurring when the spin-orbit interaction was included. No virtual molecular orbitals (MOs) were omitted in forming the CSFs. The two Jahn-Teller reference CSFs were used in all configuration interaction (CI) calculations, and sometimes additional reference CSFs to describe additional states were included. No symmetry-breaking problems occurred.

The ground- and excited-state electronic structures are characterized by 28 doubly occupied MOs. These orbitals span 11 a_1 , 4 a_2 , 5 b_1 , and 8 b_2 orbitals in C_{2v} symmetry. This leaves a total of 87 other MOs to be used by the unpaired electron and in describing correlation. Although the \tilde{X}^2E' state of Ag_3 arises from the $4d^{10}5s^1$ shells of the silver atoms, \tilde{A}^2E'' arises from the promotion of one electron from an e' MO predominantly $5s$ with some $5p_\sigma$ atomic character to an e'' MO predominantly $5p_\pi$ in character. The spin-orbit splitting is large when the open-shell MOs in the reference CSFs contain two types of $5p$ atomic orbitals (AOs) ($5p_x$ and $5p_y$ in the e' MOs, but only $5p_z$ in the e'' MOs). The spin-orbit splitting in the higher $^2E'$ states should be larger than that in the ground state due to more $5p_\sigma$ character and less $5s$

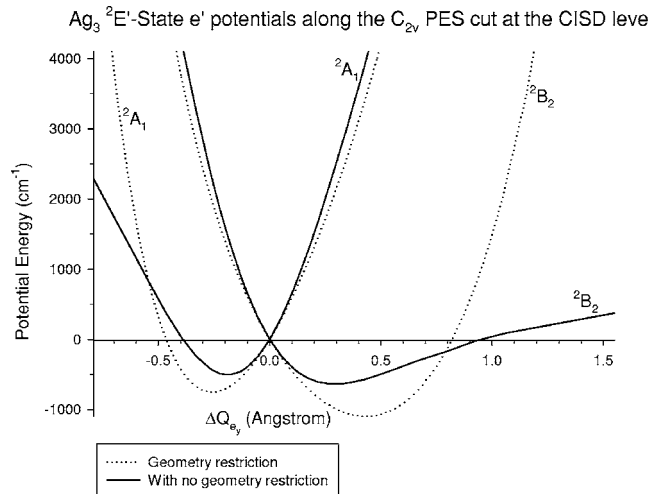


FIG. 2. Ag_3 potential energy curves for the 2A_1 and 2B_2 components of the \tilde{X}^2E' state along the C_{2v} coordinate Q_{e_y} of the single Jahn-Teller-active \tilde{X} -state e' vibrational mode. Their calculation was done at the CISD level of theory and was based on the state-averaged MOs between the Jahn-Teller-split \tilde{X} -state electronic states. The potential energy curves include the necessary correlation corrections. The global minima of the \tilde{X} -state PES correspond to potentials of the 2B_2 symmetry, while the saddle points to potentials with the 2A_1 symmetry. Note that the Jahn-Teller-split PESs cross at the symmetric configuration of Ag_3 .

character. All calculations were performed in the C_{2v} group and C_{2v} double group. Single-point calculations were conducted at the self-consistent field (SCF), singles-doubles CI (CISD), and spin-orbit CISD (SOCISD) levels of theory with the COLUMBUS suite of programs.²⁰ The MOs for the \tilde{X}^2E' state were determined by carrying out a SCF calculation using the average energy expression for the a_1^1 2A_1 and b_2^1 2B_2 states so that the MOs would be of equal quality for the Jahn-Teller-split states. The same approach was used for the \tilde{A}^2E'' state. This approach avoids symmetry-breaking problems in the electronic wave functions; the absolute energies of the Jahn-Teller-split PESs can now be directly compared, as a consequence of the fact that they may be represented (or theoretically calculated) in an equivalent manner.

The PES points of the potential energy curves were determined after Hartree-Fock geometry optimizations for C_{2v} triangular configurations, giving the geometries in Figs. 2–4 for the \tilde{X}^2E' state, and Figs. 5 and 6 for the \tilde{A}^2E'' state. Figure 5 includes similar information for a CISD geometry optimization.

The single-point calculations at the energy minima were done with the multireference singles and doubles CI (MRS-DCI) method, leading to correlated relative energies. The CI wave functions were optimized in a direct-CI iterative approach,^{22,23} employing the Davidson diagonalization method.²⁴ The Davidson correction^{25–29} was not incorporated. Either one or two roots were converged per calculation.

Past work^{10,11} formulated the electronic wave functions and energies in the framework of expansions in the complete set of wave functions at the high-symmetry point. Matrix elements with excited electronic states contribute to the quadratic Jahn-Teller terms and are referred to as causing

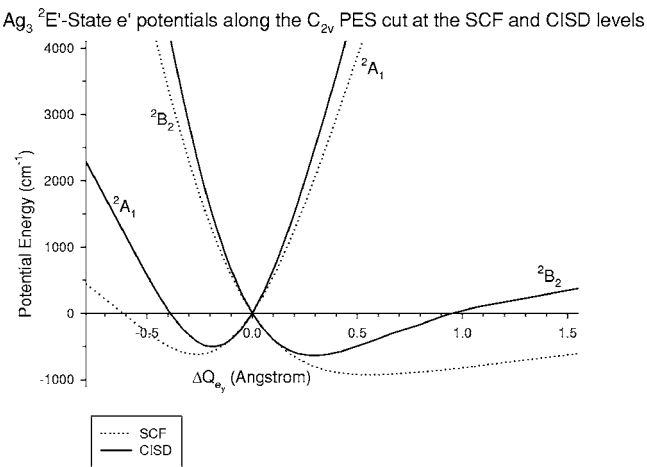


FIG. 3. Ag_3 potential energy curves at the SCF and CISD levels of theory for the $^2\text{A}_1$ and $^2\text{B}_2$ components of the $\tilde{X}^2\text{E}'$ state along the C_{2v} coordinate Q_{e_y} of the single Jahn-Teller-active \tilde{X} -state e' vibrational mode.

pseudo-Jahn-Teller mixing. The standard *ab initio* computational methods, however, do not use such expansions, but rather recompute the energies and wave functions at each geometry, thus implicitly including the pseudo-Jahn-Teller terms along with all other terms. In order to try to obtain some estimate of the magnitude of the pseudo-Jahn-Teller terms for the $\tilde{X}^2\text{E}'$ state, we made a fair number of additional single-point CISD calculations which included the reference CSFs for the lower excited electronic states of $^2\text{A}'_1$, $^2\text{A}'_2$, and $^2\text{E}'$ symmetries, corresponding to molecular analogs of the atomic $5s \rightarrow 5p_\sigma$ electron excitation. The effect on the computed Jahn-Teller PESs was to lower them somewhat in a nearly uniform manner, with almost no effect on the computed Jahn-Teller constants except to raise the barrier to pseudorotation modestly.

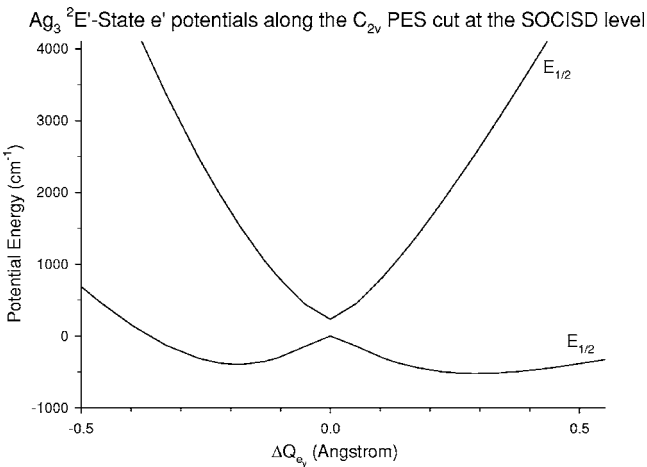


FIG. 4. Ag_3 potential energy curves at the SOCISD level of theory for the $^2\text{A}_1$ and $^2\text{B}_2$ Jahn-Teller components of the $\tilde{X}^2\text{E}'$ state along the C_{2v} coordinate Q_{e_y} of the single Jahn-Teller-active \tilde{X} -state e' vibrational mode. Note that the $^2\text{A}'_1$ and $^2\text{B}'_2$ electronic states become $E_{1/2}$ in the C_{2v} double group once the spin-orbit terms are included in the Hamiltonian; hence this designation may most appropriately be used to characterize the symmetry of the calculated potential energy curves. Note also that the inclusion of spin-orbit coupling leads to an additional energy separation between the potential energy sheets of the \tilde{X} state, most prominently depicted at the point of the symmetric trigonal configuration of Ag_3 .

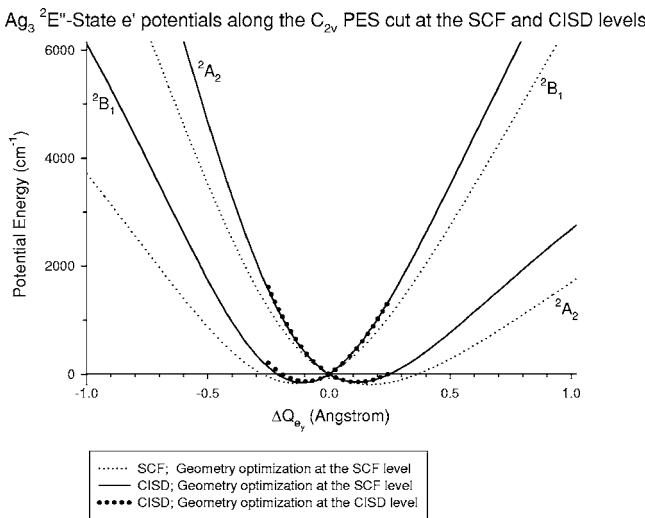


FIG. 5. Ag_3 potential energy curves at the SCF and CISD levels of theory for the $^2\text{A}_2$ and $^2\text{B}_1$ components of the $\tilde{A}^2\text{E}''$ state along the C_{2v} coordinate Q_{e_y} of the single Jahn-Teller-active \tilde{A} -state e' vibrational mode.

Additional CISD energy calculations were also performed for the $\tilde{A}^2\text{E}''$ state; the only excited state of the correct symmetry was the $^2\text{A}_2''$ state. Thus a third reference CSF was added to include all MOs based on $5p_\pi$ AOs. This required obtaining at least two roots for the $^2\text{B}_1$ calculations.

SOCISD calculations were used to measure the effect of the spin-orbit interaction on the $\tilde{X}^2\text{E}'$ - (Fig. 4) and $\tilde{A}^2\text{E}''$ -state (Fig. 6) Jahn-Teller-split potential energy curves. These calculations include electron correlation and spin-orbit effects variationally in a multireference configuration space constructed in the C_{2v} double group.

The a'_1 vibrational force constants (harmonic frequen-

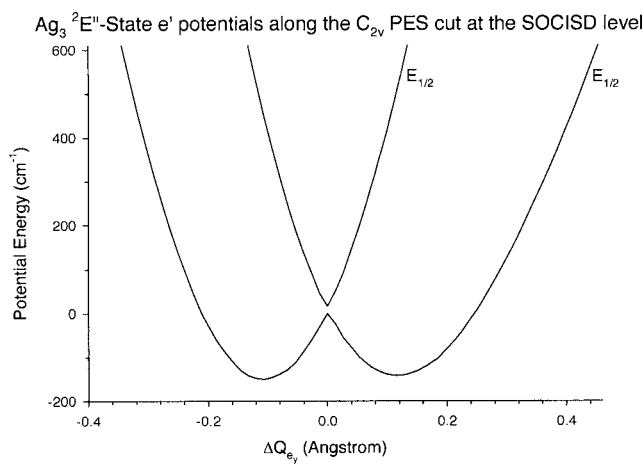


FIG. 6. Ag_3 potential energy curves at the SOCISD level of theory for the $^2\text{A}_2$ and $^2\text{B}_1$ Jahn-Teller components of the $\tilde{A}^2\text{E}''$ state along the C_{2v} coordinate Q_{e_y} of the single Jahn-Teller-active \tilde{A} -state e' vibrational mode. Note that the $^2\text{A}'_2$ and $^2\text{B}'_1$ electronic states both become $E_{1/2}$ in the C_{2v} double group once the spin-orbit terms are included in the Hamiltonian; hence this designation may most appropriately be used to characterize the symmetry of the calculated potential energy curves. Note also that the inclusion of the spin-orbit coupling leads to an additional energy separation, however smaller than in the \tilde{X} state, between the potential energy sheets of the \tilde{A} state most prominently depicted at the point of the symmetric trigonal configuration of Ag_3 .

TABLE II. Ag core cc-pVDZ basis set: $(5s5p5d1f)/[5s4p3d1f]$.

Orbital	Exponent	Contraction	Contraction	Contraction	Contraction
1s	1.080 794	-1.565 862 5	0.327 511 9	0.0	0.0
	0.869 444	1.826 103 2	-0.552 542 4	0.0	0.0
	0.096 476	0.018 721 9	0.613 864 9	1.0	0.0
	0.036 342	-0.006 117 7	0.509 576 4	0.0	1.0
3s	2.442 376	1.0			
2p	5.367 865	-0.153 662 4	0.021 639 3	0.0	0.0
	1.772 321	0.684 769 2	-0.115 531 5	-0.296 697 0	0.0
	0.670 491	0.458 797 1	-0.069 872 8	1.0	0.0
	0.118 685	0.023 950 7	0.307 010 3	0.0	-0.184 290 8
	0.030 676	-0.005 012 9	0.799 270 5	0.0	1.0
3d	2.448 778	0.297 867 0	0.0	0.0	
	1.042 491	0.449 854 5	0.0	0.0	
	0.418 454	0.346 604 9	0.0	0.0	
	0.151 913	0.132 794 7	1.0	0.0	
	0.050 700	0.000 000 0	0.0	1.0	
4f	1.541 074	1.0			

cies) of the \tilde{X}^2E' and \tilde{A}^2E'' states were calculated at the CISD level of theory imposing an equilateral geometry constraint. The two Jahn-Teller-split, state-averaged references were correlated in each case. In a second step we considered mixing between the \tilde{X}^2E' state and several other energetically close excited states. For the \tilde{X}^2E' state, the CISD calculations were repeated correlating electrons in an additional number of MOs; these span the following electronic states: $^2A_2''$ (2B_1), two $^2A_1'$ (2A_1), two $^2E'$ ($^2A_1 \oplus ^2B_2$), $^2E''$ ($^2A_2 \oplus ^2B_1$), and $^2A_2'$ (2B_2). (The spatial electronic symmetries within parentheses are for the C_{2v} symmetry reduction.) The Hartree-Fock ground-state MOs were used as an initial guess to describe the excited-state MOs. We repeated the same calculations for the two excited states of $^2E'$ symmetry that lie the closest to \tilde{A}^2E'' , but similar work was not undertaken for the latter state; while electron excitation from the atomic $4d$ shells of Ag may lead to excited electronic states with $^2E''$ symmetry, the correlation of MOs with principal or significant $4d$ atomic character was not pursued. A large series of single-point calculations was carried out at geometries along the previously described normal mode vectors.

B. Basis set construction

The basis set for Ag was constructed, having in mind three general considerations: (1) the p set should be sufficiently flexible to adequately describe the \tilde{A}^2E'' state, (2) the d set may be important in treating electron correlation, and (3) the basis set should have an economical size.

The excited state of interest arises from an electron excitation from a $5s$ -type MO to a $5p_{\pi}$ -type MO. Our effort focused on the development of a basis set that would be adequate to describe the \tilde{A}^2E'' and \tilde{X}^2E' states at equivalent levels of approximation.

The final form of the basis set for silver is displayed in Table II. We have developed a (contracted Gaussian) AO

basis set in a correlation-consistent (cc) manner,^{30,31} and it corresponds to a polarized valence double- ζ quality (cc-pVDZ) set. The resulting Ag basis set is of $(5s5p5d1f)/[5s4p3d1f]$ size, where this notation represents (primitives)/[contractions]. It was developed for use with a RECP,²¹ which replaces the atomic core electronic shells $1s^22s^22p^63s^23p^63d^{10}$ of Ag. The core orbitals are removed from such calculations, and the valence orbitals are replaced by pseudo-orbitals.³²

We used the (double- ζ in size) basis published with the RECP for testing and as a starting point for refinements, starting by minimizing the energy of the $5s^1\ ^2S$ ground state. In optimizing the set of s primitive functions for the pVDZ set,³³ we replaced one pair of duplicated exponents by a $1s$, $3s$ combination. With this change, we reoptimized all s exponents, d exponents, and the three inner p exponents, keeping the two most diffuse p exponents (suitable for the description of the $5p^1\ ^2P$ state of Ag) fixed. Following this optimization, we optimized the outer two p exponents for the 2P state, keeping all the other exponents unchanged. These optimizations were done with the program ATMSCF.³³ We then added one more d primitive to polarize the $5p$ shell and optimized it for a two-configuration SCF wave function for Ag_2 . The two most diffuse d primitives were left uncontracted. Then an f set was added to polarize and correlate the $4d$ shell, and its exponent was optimized for the SOCISD wave function for the $5s^1\ ^2S_{1/2}$ Ag state. The final basis set includes freed-up diffuse s , p , and d primitives in the same manner used in all-electron work. To avoid two-center RECP problems, we followed Christiansen's scheme³⁴ in modifying the s and p contractions.

An assessment of the accuracy of our Gaussian basis is afforded by direct comparison with the energies of the three lowest energy states of Ag. In units of cm^{-1} , the calculated excitation energies from the $^2S_{1/2}$ state to the $^2P_{1/2}$ and $^2P_{3/2}$ states are 27 458 and 28 122, compared to the experimental values³⁵ of 29 552 and 30 473, giving errors of -7.1% and

-7.7%, respectively. The spin-orbit splitting of the 2P state is calculated to be 664 compared to the experimental value of 921, giving an error of -28%. Such spin-orbit splitting values are often significantly improved with triple- ζ basis sets. One thus may anticipate moderate errors in the actual calculation of the excitation energies for Ag_3 mostly due to basis set truncation. (See Sec. V for a detailed error analysis for this work.) Despite its moderate size, this basis set should give useful results for the relative energies of the various conformations about the equilateral triangle geometry on the Ag_3 PES surface, which is the main subject of the present work.

IV. RESULTS

With the side opposite the apical Ag atom and the two equal sides of the isosceles triangle being the only two geometric factors that uniquely determine any C_{2v} structure of Ag_3 , Eq. (3) becomes

$$\mathcal{Q}_{e_y}[\alpha_1] = \frac{2}{\sqrt{6}}(\beta - \alpha), \quad (30)$$

where $\beta = r_{23}$ and $\alpha = r_{12} = r_{13}$. For any given \mathcal{Q}_{e_y} value there may only be a single pair of (α, β) for which the PES of Ag_3 becomes a minimum. The geometrically optimized C_{2v} structures for each \mathcal{Q}_{e_y} value along the PES cuts were determined as the energy minima from quadratic fits of approximately ten (α, β) pairs. The majority of the PES points were placed in the vicinity of the conical intersection and at the global minima and local maxima.

We also examined the possibility that the sum of the sides of a C_{2v} geometric conformation may deviate significantly from that defined at the optimum D_{3h} geometry, $2\alpha + \beta = 3c$, where c is the optimum D_{3h} Ag–Ag bond length.

A. The \tilde{X} state

The SCF, CISD, and SOCISD energy calculations for Ag_3 in its D_{3h} geometry led, respectively, to Ag–Ag bond lengths and correlation/spin-orbit energies of $5.4535a_0$ ($0.0000E_h$), $5.1985a_0$ (-0.9088 or $-0.9093E_h$ when more correlating MOs are used), and $5.1950a_0$ ($-0.9297E_h$) (see Table IV). The CI leads to a bond length contraction of $0.2550a_0$ in going from the SCF to the CI results, as has previously been observed in other triatomic systems,³⁶ and an additional contraction of $0.0035a_0$ in going from CI to SOCISD. A binding energy of 1.27 eV was obtained at the SOCISD D_{3h} level.

Table III summarizes the computed geometries and symmetric-stretch frequencies for the \tilde{X}^2E' state and a number of low-lying excited electronic states of Ag_3 at the D_{3h} geometry. Note that there is little variation in the bond distances for these states and that the excited states are mostly closer to each other in energy than they are to the ground state. This raises the question as to whether part of the vibronic structure in the \tilde{A}^2E'' excitation spectrum of Ag_3 (Part II) is due to interactions with neighboring electronic states (see Sec. V).

TABLE III. Summary of geometries and symmetric-stretch frequencies for the \tilde{X}^2E' state and a number of low-lying excited electronic states of Ag_3 .

State	R_e ^a CISD	a_0 CISD	ω_e (cm ⁻¹) ^b Calc.	Energy (cm ⁻¹) CISD
$^2A'_1$	5.1555		172	37 353
$^2A'_2$	5.2355		158	37 000
$^2E'^c$	5.1915 (5.1905)		163 (164)	31 811 (31 021)
\tilde{A}^2E''	5.2089		162	26 997
$^2E'^c$	5.2465 (5.2255)		161 (163)	22 503 (21 125)
$^2A'_1$	5.1855		168	18 735
$^2A''^d$	5.20		...	10 992
$\tilde{X}^2E'^c$	5.1985		161 or 165	0 or -114

^aAg–Ag distance in a.u. for an equilateral triangle geometry calculated at the CISD level of theory.

^bHarmonic frequencies, in cm⁻¹, estimated from quadratic fits to energies computed at the CISD level of theory. The a'_1 potentials of the \tilde{X}^2E' and \tilde{A}^2E'' states were found to be slightly anharmonic ($\omega_e\chi_e \leq 1$ cm⁻¹).

^cThe values in parentheses were based on CISD energy calculations where the SCF MOs converged to the excited state in question.

^dThis state was not studied in as much detail as other states.

^eThe frequency of 161 cm⁻¹ is from a CISD energy quadratic fit where the Jahn-Teller-split MOs are correlated, while the frequency of 165 cm⁻¹ is from a corresponding calculation with an extended reference list of correlating MOs.

In comparison to the \tilde{X}^2E' state's totally symmetric mode frequency, the corresponding frequencies for the excited states appear to deviate very little, assuming D_{3h} geometry. The single occupation of antibonding orbitals would in general lead to longer Ag–Ag bond lengths for the D_{3h} structures. This in turn would indicate lower vibrational frequencies. This happens for several of the excited states. However, the bond lengths of the \tilde{X}^2E' state and the excited $^2E'$ state above the \tilde{A}^2E'' state are comparable, which further suggests that the bond order of Ag_3 is little affected by the higher MO occupation. The bond lengths for the D_{3h} structures of the other excited states near \tilde{A}^2E'' are comparable and the symmetric-stretch frequencies are similar.

Figure 2 presents the Jahn-Teller-split potential energy curves of 2A_1 and 2B_2 symmetries as a function of the displacement coordinate $\Delta\mathcal{Q}_{e_y}$ (in angstroms), calculated at the CISD level. Note that the $^2E'$ point is a local maximum on the PES with distortion to C_{2v} symmetry leading to a lowering in the energy for both 2A_1 (local minimum) and 2B_2 (global minimum) symmetries. The 2A_1 symmetry favors narrow-angle geometries, while the 2B_2 symmetry favors wide-angle geometries. A comparison between the dotted (with geometry restriction) and solid (with no geometry restriction) lines suggests that the approximation of keeping the totally symmetric coordinate R constant at its value at the molecule's equilibrium point is valid only for areas of the PES that lie close to the conical intersection. The 2B_2 surface shows a marked asymmetry (solid line) leading to a linear $^2S_u^+$ state as $\Delta\mathcal{Q}_{e_y}$ becomes larger. The 2A_1 and 2B_2 surfaces appear to be relatively shallow. Thus the wide-angle structure has an apex angle of 69° (global minimum and 2B_2 symmetry), while the narrow-angle structure has an apex angle of 55° (saddle point and 2A_1 symmetry.) A summary of the Ag–Ag bond lengths for the apical side R_e (23) and the

TABLE IV. Geometries and energy separation of the \tilde{X}^2E' and \tilde{A}^2E'' Jahn-Teller-split states of Ag_3 .

	Electronic symmetry ^a	$R_e(12)$ (Å)	$R_e(23)$ (Å)	θ_e (deg)	ΔE (cm ⁻¹) ^b
\tilde{X}^2E' state	($^2E'$) ^c	2.8859	2.8859	60	0
	($^2E'$) ^d	2.7509	2.7509	60	
	($^2E'$) ^e	2.7491	2.7491	60	
	2B_2	2.8161	3.1725	69	-633
	2A_1	2.9849	2.7581	55	-504
\tilde{A}^2E'' state	($^2E''$) ^c	2.8857	2.8857	60	0
	($^2E''$) ^{d,e}	2.7564	2.7564	60	
	2A_2	2.8483	2.9901	63	-150
	2B_1	2.9353	2.8057	57	-158

^aThe geometries at the stationary points and at the high-symmetry point of the \tilde{X}^2E' and \tilde{A}^2E'' Jahn-Teller-distorted PESs of Ag_3 . The positions of the stationary points (Hartree-Fock geometry optimized structures) do not change upon inclusion of the spin-orbit correction. For the \tilde{X} -state PES, the global minimum is predicted to be at ρ_{\min} (Å)=0.29 and the saddle point at ρ_{\max} (Å)=−0.18. For the \tilde{A} -state PES, the global minimum and saddle point are found at ρ_{\min} (Å)=−0.11 and ρ_{\max} (Å)=0.12, respectively.

^bThe zero energy corresponds to the Hartree-Fock geometry optimized D_{3h} structure of Ag_3 in its \tilde{X}^2E' and \tilde{A}^2E'' states. The barrier to pseudorotation for the \tilde{X}^2E' state is 129 cm^{−1}, while for the \tilde{A}^2E'' state it is 8 cm^{−1}.

^cGeometry optimization for a D_{3h} structure at the SCF level of theory.

^dGeometry optimization for a D_{3h} structure at the CISD level of theory.

^eGeometry optimization for a D_{3h} structure at the SOCISD level of theory.

two equal sides $R_e(12)$ of the isosceles triangle at the stationary points of the Jahn-Teller-distorted \tilde{X} -state PES is given in Table IV.

While the qualitative characteristics of the SCF potential energy curves remain the same upon inclusion of CI, there are large quantitative effects of correlation as shown in Fig. 3, where the CI curves have been raised to have the same crossing point as the SCF curves. The CISD displacements in the Q_{e_y} coordinate to reach the stationary points are smaller than the SCF values. In particular, the 2B_2 surface becomes considerably less flat upon inclusion of correlation. The energy separation between the conical intersection and the global minimum of the 2B_2 state is 633 cm^{−1}, while the value for the saddle point of the 2A_1 state is 504 cm^{−1}, making the barrier to pseudorotation around the moat 129 cm^{−1}. The lowest (coupled) vibrational state is calculated to be 456 cm^{−1} below the conical intersection, somewhat above the barrier. With experimentally fit parameters (Part II), this value changes to 448 cm^{−1}.

Figure 4 shows the theoretically calculated Jahn-Teller-split potential energy curves of Ag_3 in the presence of spin-orbit coupling. The two effects have opposite actions on the geometry; the spin-orbit coupling may quench the Jahn-Teller distortion if it is considerably greater than the latter. We noted earlier that for the \tilde{X}^2E' (D_{3h}) state of Ag_3 , the Ag–Ag bond length is subject to a relativistic contraction, but that the effect of spin-orbit interaction on the geometry is minimal for Ag_3 in its \tilde{X} state. When considering spin-orbit coupling, the D_{3h} symmetry at the conical intersection turns into the D_{3h}^2 double group symmetry; hence the $^2E'$ electronic state in D_{3h} symmetry is split into the $E_{3/2}$ and $E_{5/2}$ spin-orbit components, with the latter having a lower energy. Both of these spin components transform like $E_{1/2}$ in the C_{2v} double group. In Fig. 4, the zero of energy was set at the D_{3h} energy of the lower curve. The energy separation at the sym-

metric configuration point of the \tilde{X} -state PES due to spin-orbit coupling is 232 cm^{−1}. A comparison between the CISD-calculated potential energy curves of Fig. 3 and the ones of Fig. 4 after having subtracted out their energy difference at the symmetric configuration due to the spin-orbit interaction leads to approximately a set of overlapping potential energy curves. The positions of the stationary points in the Jahn-Teller-distorted PES of the \tilde{X} state do not change upon inclusion of the spin-orbit interaction, nor does their relative energy difference since the PES points along the potential energy curves have been determined after a geometry optimization at the Hartree-Fock level and not at the SOCISD level. So the spin-orbit coupling is merely incorporated as a final correction to the PES.

In Sec. II C we gave our general theoretical methodology which was based on a second-order truncated expression for the general Hamiltonian given in Eq. (7). This approximation led to Eq. (12) which pertains to the cut of the global PES along the Q_{e_y} coordinate. Such an approach is based on what has previously been classified as the dominant Jahn-Teller vibronic interactions. Using Eqs. (23)–(25) we obtained

$$\lambda_{e'} \text{ (cm}^{-1}/\text{\AA}^2\text{)} = 25\,951,$$

$$k_{e'} \text{ (cm}^{-1}/\text{\AA}\text{)} = 5253,$$

$$g_{e'} \text{ (cm}^{-1}/\text{\AA}^2\text{)} = 1908.$$

Using Eqs. (14)–(16), we obtained

$$\omega_{e,e'} \text{ (cm}^{-1}\text{)} = 156,$$

$$D_{e'} = 3.41,$$

$$K_{e'} = 0.07.$$

The quadratic Jahn-Teller constant compares well with the one calculated from Eq. (26); with $E_{e'}^0$ (cm^{-1}) = -633 and $E_{e'}^{\pi/3}$ (cm^{-1}) = -504, Eq. (26) predicts $K_{e'} = 0.06$. Using Eqs. (18)–(22), we obtained

$$\rho_{e'}^0 (\text{\AA}) = 0.23,$$

$$E_{e'}^0 (\text{cm}^{-1}) = -613,$$

$$\rho_{e'}^{\pi/3} (\text{\AA}) = -0.18,$$

$$E_{e'}^{\pi/3} (\text{cm}^{-1}) = -469,$$

$$\Delta E_{e'}^B (\text{cm}^{-1}) = 144.$$

(The minus sign in $\rho_{e'}^{\pi/3}$ is due to the $\cos \phi$ dependence.) This set of parameters compares well with the CISD results of Fig. 2,

$$\rho_{e'}^0 (\text{\AA}) = 0.29,$$

$$E_{e'}^0 (\text{cm}^{-1}) = -633,$$

$$\rho_{e'}^{\pi/3} (\text{\AA}) = -0.18,$$

$$E_{e'}^{\pi/3} (\text{cm}^{-1}) = -504,$$

$$\Delta E_{e'}^B (\text{cm}^{-1}) = 129.$$

However, other workers¹² have recently pointed out that for Ag_3 cubic contributions can become important to the warping of the APES of the \tilde{X}^2E' state. It is worthwhile to investigate this possibility further.

García-Fernández *et al.*¹² derived general formulas that take into consideration linear, quadratic, and cubic contributions to the APES, which we make use of. We find that the dominant mechanism of warping in the \tilde{X}^2E' -state Jahn-Teller APES is due to the linear terms, as will be shown in detail later. If all terms up to ρ^3 are included in the effective Hamiltonian, Eq. (12) becomes

$$\begin{aligned} V_{\pm, e'}^{l, q} &= \frac{1}{2}\lambda_{e'}\rho^2 + \frac{1}{2}c_{e'}\rho^3 \cos(3\phi) \\ &\pm k_{e'}\rho \left(1 + \frac{2g_{e'}\rho}{k_{e'}} \cos(3\phi) + \frac{g_{e'}^2\rho^2}{k_{e'}^2} + \frac{2m_{e'}\rho^2}{k_{e'}} \right)^{1/2} \\ &\approx \frac{1}{2}\lambda_{e'}\rho^2 + \frac{1}{2}c_{e'}\rho^3 \cos(3\phi) \pm \left(k_{e'}\rho + g_{e'}\rho^2 \cos(3\phi) \right. \\ &\quad \left. + \frac{1}{8}\frac{g_{e'}^2\rho^3}{k_{e'}}(1 - \cos(6\phi)) + m_{e'}\rho^3 \right) \\ &\approx \frac{1}{2}\lambda_{e'}\rho^2 + \frac{1}{2}c_{e'}\rho^3 \cos(3\phi) \end{aligned}$$

$$\pm [k_{e'}\rho + g_{e'}\rho^2 \cos(3\phi) + m_{e'}\rho^3]. \quad (31)$$

In the above equations $c_{e'}$ and $m_{e'}$ represent¹² the cubic anharmonicity and the cubic Jahn-Teller coupling constant of the e' mode, respectively. In the last equation, terms that involve $\cos(6\phi)$ have been neglected, as no evidence of significant contribution from such terms has previously been documented.¹² This assumption is also confirmed from the fit of our own *ab initio* results to such expressions, which show that the contribution from the $m_{e'}$ terms is negligible.

The positions of the stationary points of the \tilde{X} -state PES do not change upon full inclusion of interactions with nearby excited electronic states (the global minimum remains at 0.29 Å, while the local maximum changes to -0.17 from -0.18 Å). Then using Eqs. (31),

$$\left(\frac{dV_+}{d\rho} \right)_{\max} = 0 \quad (32)$$

and

$$\left(\frac{dV_-}{d\rho} \right)_{\min} = 0. \quad (33)$$

We obtain

$$\lambda_{e'}\rho_{\min} + \frac{3}{2}c_{e'}\rho_{\min}^2 - k_{e'} - 2g_{e'}\rho_{\min} = 0, \quad (34)$$

$$\lambda_{e'}\rho_{\max} + \frac{3}{2}c_{e'}\rho_{\max}^2 + k_{e'} + 2g_{e'}\rho_{\max} = 0. \quad (35)$$

Adding Eqs. (34) and (35) gives

$$\begin{aligned} \lambda_{e'}(\rho_{\min} + \rho_{\max}) + \frac{3}{2}c_{e'}(\rho_{\min}^2 + \rho_{\max}^2) \\ + 2g_{e'}(\rho_{\max} - \rho_{\min}) = 0. \end{aligned} \quad (36)$$

Hence with the CISD-calculated values for the positions of the stationary points of the \tilde{X} state ($\rho_{\min} = 0.29$ Å and

TABLE V. Molecular parameters of the \tilde{X}^2E' electronic state of Ag_3 (The conversion factor used is 1 mdyn = 50 341.1762 $\text{cm}^{-1}/\text{\AA}$.)

Variable (units)	
Atomic weight of Ag (amu)	107.8682
Force constant $\lambda_{e'}$ ($\text{cm}^{-1}/\text{\AA}^2$)	25 951
Force constant $\lambda_{e'}$ (mdyn/Å)	0.52
Frequency of $\nu_2(e')$ (cm^{-1})	156
Cubic anharmonicity $c_{e'}$ ($\text{cm}^{-1}/\text{\AA}^3$)	-6206
Cubic anharmonicity $c_{e'}$ (mdyn/Å ²)	-0.12
Linear Jahn-Teller constant $k_{e'}$ ($\text{cm}^{-1}/\text{\AA}$)	5253
Linear Jahn-Teller constant $k_{e'}$ (mdyn)	0.10
Linear Jahn-Teller constant $D_{e'}$	3.41
Quadratic Jahn-Teller constant $g_{e'}$ ($\text{cm}^{-1}/\text{\AA}^2$)	1720
Quadratic Jahn-Teller constant $g_{e'}$ (mdyn/Å)	0.034
Quadratic Jahn-Teller constant $K_{e'}$	0.07
Bilinear Jahn-Teller constant $b_{a'_1 e'}$ (cm^{-1})	-1
Bilinear Jahn-Teller constant $B_{a'_1 e'}$	-0.01
Force constant of $\lambda_{a'_1}$ ($\text{cm}^{-1}/\text{\AA}^2$) ^a	28 955
Force constant of $\lambda_{a'_1}$ (mdyn/Å) ^a	0.57
Frequency of $\nu_1(a'_1)$ (cm^{-1}) ^a	165
Spin-orbit coupling (cm^{-1})	232

^aDerived based on a CISD wave function with an extended reference space of correlating MOs.

TABLE VI. Mulliken population analysis for Ag_3 (M_2 refers to the two base atoms of the isosceles triangle of Ag_3 . These results pertain to the position of the stationary points in the Jahn-Teller-distorted PES of the \tilde{X}^2E' and \tilde{A}^2E'' states.)

State	M	Gross						
		M_2	$M(s)$	$M_2(s)$	$M(p)$	$M_2(p)$	$M(d)$	$M_2(d)$
\tilde{X}^2E'	2B_2	18.91	38.08	2.69	5.82	6.25	12.30	9.98
	2A_1	19.13	37.87	3.01	5.49	6.15	12.43	9.98
\tilde{A}^2E''	2B_1	19.28	37.72	2.53	5.24	6.84	12.57	9.92
	2A_2	18.71	38.29	2.65	5.12	6.10	13.31	9.96

$\rho_{\max} = -0.18 \text{ \AA}$ in Fig. 2) given, and once $\lambda_{e'}$ and $c_{e'}$ are calculated, then Eq. (36) can be used to calculate $g_{e'}$. Although $\lambda_{e'}$ and $c_{e'}$ may be calculated at a satisfactory level of confidence, the fitting error may primarily affect $c_{e'}$ and it unavoidably propagates into $g_{e'}$.

Upon inclusion of the e' cubic anharmonicity, and omitting the $m_{e'}$ terms due to their negligible magnitude, Eqs. (23) and (24) become

$$V_+ + V_- \approx \lambda_{e'} \rho^2 + c_{e'} \rho^3, \quad (37)$$

$$(V_+ - V_-)/2 \approx k_{e'} \rho + g_{e'} \rho^2. \quad (38)$$

By fitting the CISD energies to the PES points lying at the vicinity of the conical intersection, we derive

$$\lambda'_{e'} (\text{cm}^{-1}/\text{\AA}^2) = 25\,951,$$

$$c_{e'} (\text{cm}^{-1}/\text{\AA}^3) = -6202,$$

$$k_{e'} (\text{cm}^{-1}/\text{\AA}) = 5253.$$

The linear Jahn-Teller constant $k_{e'}$ remains practically the same when a larger grid of PES points is used for the fit, i.e., the space of PES points connecting the stationary points. The only new calculated parameter here is $c_{e'}$, with $\lambda_{e'}$ and $k_{e'}$ remaining the same. Having values for $\lambda_{e'}$ and $c_{e'}$, we return to Eq. (36) and calculate $g_{e'}$

$$g_{e'} (\text{cm}^{-1}/\text{\AA}^2) = 1720. \quad (39)$$

If we go back to Eqs. (14)–(16) and Eqs. (18)–(22) we obtain the same set of fit values as before. Equations (14)–(22) were derived assuming a second-order truncation for the Taylor series expansion of the electronic Hamiltonian. These equations, hence, strictly represent the linear and quadratic contributions to the topology of the APES in the $E \otimes e$ problem. The fit values do not change when we include the cubic contribution, which is small enough to have almost no effect on the PES. The major contributions to the topology of the APES is due to the linear contribution and in part due to the quadratic contribution, since these alone suffice to adequately represent the topographic characteristics of the Jahn-Teller-distorted PES. Table V summarizes all of the theoretically derivable parameters for the \tilde{X}^2E' state of Ag_3 .

Table VI shows the SCF Mulliken population analysis of Ag_3 calculated at the stationary points of the Jahn-Teller-distorted \tilde{X}^2E' PES. In the 2B_2 state a total charge transfer of $0.08e$ from the apex Ag atom to the base Ag atoms is observed, whereas in the 2A_1 state $0.13e$ have moved from the

base Ag atoms to the apex Ag atom. Hence, in the 2B_2 state the apex Ag atom carries a positive charge, while in the 2A_1 state it carries a negative charge. The dipole moment of the $^2E'$ state (D_{3h} geometry) is zero, so the dipole moments of the two \tilde{X} -state Jahn-Teller components should have opposite signs. Our observations confirm this, and are in agreement with previous work.^{1,37}

Table VI also indicates that for the \tilde{X}^2E' -state Jahn-Teller-split electronic states, the bonding is mainly due to the $5s$ - $5p$ electrons. The deviation of the total d populations from the expected valence value of 30 suggests that the $4d$ electrons participate in the bonding to some extent. The contributions from d electrons in both of the \tilde{X}^2E' Jahn-Teller-split electronic states are similar. The participation of the $5p$ AOs is indeed important here. This is readily explained based on the atomic states of Ag.³⁵ While the first excited state of Ag is due to the $4d^{10}5p$ configuration and lies approximately $30\,000 \text{ cm}^{-1}$ above the ground electronic state, the excited states due to the $4d^95s^2$ configuration are at approximately $30\,300$ – $35\,000 \text{ cm}^{-1}$, but the $5p$ orbitals have a similar radial extent to that of the $5s$ orbitals, while the $4d$ orbitals are significantly more compact. Thus, as others have previously noticed,^{37,38} the $5p$ orbitals participate more in the bonding of Ag_3 than the $4d$ orbitals.

TABLE VII. Molecular parameters of the \tilde{A}^2E'' electronic state of Ag_3 (The conversion factor used is $1 \text{ mdyn} = 50\,341.1762 \text{ cm}^{-1}/\text{\AA}$.)

Variable (units)	
Atomic weight of Ag (amu)	107.8682
Force constant $\lambda_{e'} (\text{cm}^{-1}/\text{\AA}^2)$	25 613
Force constant $\lambda_{e'} (\text{mdyn}/\text{\AA})$	0.51
Frequency of $\nu_2(e')$ (cm^{-1})	155
Linear Jahn-Teller constant $k_{e'} (\text{cm}^{-1}/\text{\AA})$	2801
Linear Jahn-Teller constant $k_{e'} (\text{mdyn})$	0.06
Linear Jahn-Teller constant $D_{e'}$	0.99
Quadratic Jahn-Teller constant $g_{e'} (\text{cm}^{-1}/\text{\AA}^2)$	-247
Quadratic Jahn-Teller constant $g_{e'} (\text{mdyn}/\text{\AA})$	-0.005
Quadratic Jahn-Teller constant $K_{e'}$	-0.01
Bilinear Jahn-Teller constant $b_{a'_1e'} (\text{cm}^{-1})$	-1
Bilinear Jahn-Teller constant $B_{a'_1e'}$	-0.01
Force constant of $\lambda_{a'_1} (\text{cm}^{-1}/\text{\AA}^2)^a$	28 135
Force constant of $\lambda_{a'_1} (\text{mdyn}/\text{\AA})^a$	0.56
Frequency of $\nu_1(a'_1)^a$	162
Spin-orbit coupling (cm^{-1})	17

^aDerived based on a CISD wave function with an extended reference space of correlation MOs.

B. The \tilde{A} state

The \tilde{A}^2E'' -state SCF and CISD energy calculations gave Ag–Ag bond lengths of $5.4532a_0$ and $5.2089a_0$, respectively. The spin-orbit interaction had no effect on the geometry. The bond length contraction in going from SCF to CI or SOCISD was $0.2443a_0$. The symmetric-stretch frequency was calculated to be 162 cm^{-1} (Table III).

Figure 5 shows the \tilde{A}^2E'' -state Jahn-Teller-split potential energy curves of 2A_2 and 2B_1 symmetries, expressed in units of cm^{-1} , as a function of the displacement coordinate ΔQ_{e_y} (in angstrom). The dotted lines were calculated at the SCF level of theory after a SCF geometry optimization. The CISD energy calculations gave the solid lines and the intensely dotted lines which, respectively, are based on the SCF and CISD geometry optimizations.

While the 2A_2 state favors wide-angle geometries, the 2B_1 state favors narrow-angle geometries. Based on the “solid-line” calculations, the global minimum is located in the potential of the 2B_1 state and is characterized by a narrow-angle structure with an apex angle of 57° , while the saddle point is located on the potential of the 2A_2 state and corresponds to a wide-angle structure with an apex angle of 63° . The energy of the global minimum (relative to the conical intersection) (at $\rho_{\min}=-0.11\text{ \AA}$) is -158 cm^{-1} and that of the saddle point (at $\rho_{\max}=0.12\text{ \AA}$) is -150 cm^{-1} . The barrier to pseudorotation is 8 cm^{-1} . The Ag–Ag bond lengths $R_e(12)$ and $R_e(23)$ of the molecule’s C_{2v} configurations at the stationary points of the Jahn-Teller-distorted \tilde{A}^2E'' state PES are presented in Table IV. No significant quadratic Jahn-Teller activity is expected based on the \tilde{A}^2E'' state’s theoretically calculated topological characteristics of the Jahn-Teller-distorted PES; the stationary points are almost isoenergetic and at a nearly equal displacement from the conical intersection. We also note that smaller displacement vectors are required to reach the stationary points with the CI results compared to the SCF results. We checked the approximation of using Hartree-Fock geometry optimization and conducted a CISD geometry optimization but only for a limited section of the PES, the region in the immediate vicinity of the conical intersection. In comparing our newly acquired potential lines (intensely dotted) with the solid-line CISD curves, we found no significant deviation.

Some additional calculations were conducted. We compared our geometry-restricted and unrestricted potential lines and found that for the CISD calculations at optimized SCF geometries, it is not a good approximation to assume R to be a constant along the Q_{e_y} cut of the \tilde{A}^2E'' -state PES.

Figure 6 shows the \tilde{A}^2E'' -state Jahn-Teller-split potentials of Ag_3 in the presence of spin-orbit coupling. When considering spin-orbit coupling, the $^2E''$ electronic state in D_{3h} symmetry is split into $E_{3/2}$ and $E_{1/2}$ spin-orbit components. They both transform like $E_{1/2}$ in the C_{2v} double group. The energy separation between the Jahn-Teller-split \tilde{A}^2E'' -state lines at the symmetric configuration point in the presence of the spin-orbit interaction is 17 cm^{-1} . Such a

small energy separation is consistent with the observation of a negligible effect of the spin-orbit interaction on the geometry of Ag_3 in the \tilde{A}^2E'' state.

Based on Eqs. (23)–(25), the following set of parameters is calculated for the \tilde{A}^2E'' state:

$$\lambda_{e'} (\text{cm}^{-1}/\text{\AA}^2) = 25\,613,$$

$$k_{e'} (\text{cm}^{-1}/\text{\AA}) = 2801,$$

$$g_{e'} (\text{cm}^{-1}/\text{\AA}^2) = -247.$$

Equations (14)–(16) give

$$\omega_{e,e'} (\text{cm}^{-1}) = 155,$$

$$D_{e'} = 0.99,$$

$$K_{e'} = -0.01.$$

Equation (26) (with $E_{e'}^0 = -150\text{ cm}^{-1}$ and $E_{e'}^{\pi/3} = -158\text{ cm}^{-1}$) predicts $K_{e'} = -0.01$. By using Eqs. (18)–(22) we obtain

$$\rho_{e'}^0 (\text{\AA}) = 0.11,$$

$$E_{e'}^0 (\text{cm}^{-1}) = -150,$$

$$\rho_{e'}^{\pi/3} (\text{\AA}) = -0.11,$$

$$E_{e'}^{\pi/3} (\text{cm}^{-1}) = -156,$$

$$\Delta E_{e'}^B (\text{cm}^{-1}) = 6.$$

(The minus sign in $\rho_{e'}^{\pi/3}$ is due to the $\cos \phi$ dependence.) The above set of parameters is in agreement with the solid-line CISD results

$$\rho_{e'}^0 (\text{\AA}) = 0.12$$

$$E_{e'}^0 (\text{cm}^{-1}) = -150,$$

$$\rho_{e'}^{\pi/3} (\text{\AA}) = -0.11,$$

$$E_{e'}^{\pi/3} (\text{cm}^{-1}) = -158,$$

$$\Delta E_{e'}^B (\text{cm}^{-1}) = 8.$$

As a final remark, we note that the major contribution to the topology of the APES of the \tilde{A}^2E'' state comes from the linear Jahn-Teller term; the quadratic and cubic contributions have little effect. The PES fit along R and Q_{e_y} gave $b_{a'_1 e'} (\text{cm}^{-1}) = -1$, which corresponds to $B_{a'_1 e'} = -0.01$ based on Eq. (17). Table VII summarizes the calculated parameters for the \tilde{A}^2E'' state of Ag_3 .

Table VI presents the SCF Mulliken population analysis at the stationary points of the Jahn-Teller-distorted \tilde{A}^2E'' PES. A charge transfer of $0.29e$ from the apex Ag atom to the base Ag atoms is observed in the 2A_2 state. In the 2B_1 state,

$0.28e$ moves from the base Ag atoms to the apex Ag atom. The charge distribution confirms the center of gravity rule with respect to the signs of the dipole moments arising from the \tilde{A} -state Jahn-Teller components. The bonding involves principally $5s$ - $5p$ AOs. The involvement of $4d$ AOs is now greater than in the \tilde{X}^2E' state.

V. DISCUSSION

The primary focus of this theoretical investigation was to calculate reliable Jahn-Teller parameters which can be used as starting points for the Jahn-Teller spectral simulations. The theoretical parameters can in turn be refined by using experimental data. From the comparison of our theoretical parameters with the experimental ones (see Part II), we find that they are generally in good agreement for both the \tilde{X}^2E' and \tilde{A}^2E'' states. However, as will be seen in Part II, the Jahn-Teller calculations are successful in reproducing the pattern of the experimentally observed vibronic energy levels only when the quadratic Jahn-Teller constant is fit experimentally, particularly for the \tilde{A}^2E'' state.

Upon inclusion of relativistic effects, all electronic states span the same irreducible representation in the C_{2v} double group, $E_{1/2}$. All these can mix due to the spin-orbit matrix elements, and this mixing becomes more important in energy regions where the congestion is high. It may be that higher-order excitations become important for the \tilde{A}^2E'' -state PES. Although we did not find them to have a significant impact, it is possible that extending the virtual space (using a larger basis set) and including references with $4d$ excitations would reveal stronger mixing.

Of particular interest is the consideration of the possible errors in our theoretical calculations. There are errors due to the incompleteness of the basis set, the computational methodology, and the description of the relativistic effects in the system. A central question is how accurate the relative energies of the C_{2v} structural isomers of Ag_3 are.

Our fundamental approach was to conduct a geometry optimization at the Hartree-Fock level, then as a second step include the correlation effects and at the end incorporate the effect of the spin-orbit interaction (which is admittedly the least important factor in Ag_3 ³⁷). Although the energies of the potential energy curves relative to the conical intersection are not expected to significantly deviate upon inclusion of correlation effects at the geometry optimization step (we rigorously tested this assumption for the \tilde{A}^2E'' -state Jahn-Teller-split potentials, and it was proven correct), the minimum energy geometries themselves along the potentials will be different. The MRSDCI methodology is bound by the size-consistency effects, as in the MRSDCI wave function higher-order excitations are not fully accounted for. The magnitude of the error for Ag_3 may be estimated from its effect on the Ag–Ag bond lengths. Indeed, we made small changes in the minimum energy geometries (located at the CISD level of theory), and found that the size-consistency effects do not substantially distort the \tilde{X}^2E' - and \tilde{A}^2E'' -state PESs. We believe that our theoretical calculations on Ag_3 treat the electron correlation to a good accuracy for a molecule containing

57 electrons. Experience with similar systems³⁶ also suggests that the size-consistency error is not the major computational error here. We believe that our SOCISD methodology adequately described the electronic structure of Ag_3 , as the main features of the Ag_3 PES were readily confirmed from the experimental data. The relativistic effects are mainly introduced by the RECPs and by the use of the spin-orbit operators in our calculations; it has earlier been shown that the effect of spin-orbit interaction is underestimated here. The spin-orbit splitting in the \tilde{X}^2E' and \tilde{A}^2E'' states is predicted to be small; furthermore, it is effectively quenched in both states by the Jahn-Teller activity. Hence, any errors in the spin-orbit treatment do not lead to significantly different results from those obtained in our experimental analysis of Part II.

The size-consistency effects will not greatly affect the calculated excitation energies, since the size-consistency error remains approximately constant when comparing the energies between the \tilde{X}^2E' state and several other excited electronic states for Ag_3 at its D_{3h} geometry (see Table III). A larger basis set is needed for a theoretical test of our predicted excitation energy spectrum for Ag_3 . The good prediction for the $\tilde{X}^2E' \rightarrow \tilde{A}^2E''$ excitation energy may result from fortuitous cancellation of errors. Our calculated excited-state energies may be of additional use; based on our excitation-spectrum experimental results (Part II), a pattern of increasing vibronic-level congestion is observed in the spectral region to the blue of the $\tilde{A}^2E'' \leftarrow \tilde{X}^2E'$ origin which may be due to the vibronic energy level structure of the $^2E'$ electronic state lying higher than the \tilde{A}^2E'' state.

In this work we focused our attention on C_{2v} cross sections of the \tilde{X}^2E' - and \tilde{A}^2E'' -state PESs without performing additional calculations for non- C_{2v} potential energy points because these cross sections determined all the needed potential parameters. The agreement with the experimental observations is sufficient to indicate that additional geometry points are unnecessary (see Part II). In the pseudorotation process, only C_{2v} structures are involved at the stationary points. This also occurred for the \tilde{X}^2E' state of Cu_3 .³⁶ Table VIII summarizes the present and past work regarding the geometries of Ag_3 at the global minima and saddle points as well as at the conical intersection of the Jahn-Teller-distorted PES of the \tilde{X}^2E' electronic state. Our work's calculated apex angles for the C_{2v} structures of the 2B_2 and 2A_1 electronic states are in good agreement with previous studies, as are the Ag–Ag bond lengths, which will probably contract somewhat further if correlation is incorporated into the geometry optimization process, which we only slightly investigated in our work.

The $4d$ shell of Ag is expected to remain atomiclike, but the $4d$ electrons are not inert, since correlating them shortens the bonds of Ag_3 (see Table IV). This finding is consistent with previous work on similar systems.^{36,37,39,40} The bond lengths are expected to shorten further due to higher-order excitations which were not included in the present MRSDCI methodology. We have observed a relativistic contraction on the Ag–Ag bond lengths of the equilateral Ag_3 triangle in its

TABLE VIII. Geometries of Ag_3 at the global minima and saddle points as well as at the conical intersection of the Jahn-Teller-distorted PES of the \tilde{X}^2E' electronic state. Comparison of the present results with past theoretical studies in reverse chronological order.

	2B_2		2A_1		$^2E'$
	$R_e(12)$ (Å)	θ_e (deg)	$R_e(12)$ (Å)	θ_e (deg)	R_e (Å) ^a
Present work	2.8161	69	2.9779	55	2.7509
Ref. 12	2.771
Ref. 1	2.593	70.45	2.758	55.08	2.670
Ref. 45	2.774	68.54	2.948	54.92	2.849
Ref. 2	2.695	67.88	2.846	55.43	...
Ref. 46	2.687	69.1	2.892	54.1	...
Refs. 47 and 48	2.709	69.2
Ref. 37	2.72	63.7	2.88	54.2	...
Ref. 38	2.709	69.2	2.885	55.2	...
Ref. 49	2.582	67.5	2.725	55.2	...

^aThe Ag–Ag bond distance at the D_{3h} geometry.

\tilde{X}^2E' state, but not in its \tilde{A}^2E'' state. This is expected; orbitals that have significant density near the nucleus are subject to an increased relativistic contraction. Hence s orbitals are expected to contract the most. Ag_3 in its \tilde{X}^2E' state (D_{3h} symmetry) has a shorter bond length (2.7491 Å in Table IV, larger totally symmetric vibrational frequency expected) than in its \tilde{A}^2E'' state (2.7564 Å), since the $5s$ orbital is less diffuse than the $5p$ orbital. The small magnitude of the relativistic effects in Ag_3 also explains the relatively small contraction of the bond length in the D_{3h} configuration of the \tilde{X}^2E' state and the lack of any additional contraction due to relativity for the corresponding D_{3h} configuration of \tilde{A}^2E'' .

Ag_3 is among the Ag clusters that have shown the greatest ambiguity. Previous gas-phase and matrix-isolation experimental studies have reported on the frequencies of Ag_3 in its \tilde{X}^2E' and \tilde{A}^2E'' states.⁴¹ Briefly, one observes a discrepancy between the gas-phase and the matrix-isolation values for the totally symmetric and degenerate bend frequencies. However, it must be pointed out that the totality of the suggested gas-phase values for the totally symmetric frequency converges mostly to $\approx 160 \text{ cm}^{-1}$ for the \tilde{X}^2E' and \tilde{A}^2E'' states.

Lombardi and Davis⁴¹ have taken a somewhat different approach on the matter of calculating a reliable frequency for the totally symmetric mode of Ag_3 ; they estimated the force constants (hence the totally symmetric frequencies) of Ag_3 and various other silver clusters based on actual experimental data, having in mind the scheme proposed by Ozin and McIntosh,⁴² which predicts the force constants of higher clusters from that of the dimer. Using information for the ground state⁴³ of Ag_2 , i.e., ${}^1\Sigma_g^+(0_g^+)$, $\omega_e (\text{cm}^{-1}) = 192.4(5)$ or force constant of 1.18 mdyne/Å (59 403 cm⁻¹/Å²), Lombardi and Davis estimated the ground-state bond stretching a force constants of Ag_n with $n=5, 7, 9, 13$ based on the existing spectra.⁴¹ They also applied Ozin and McIntosh's scheme and were able to predict the bond stretching force constants for these species as well as the one for the ambiguous Ag_3 . There was good correlation between the experimentally found and predicted values for the force constants. Thus it is

likely that the predicted value of 0.59 mdyne/Å (29 701 cm⁻¹/Å² or 167 cm⁻¹) for the ground-state force constant of Ag_3 , which also agrees with the gas-phase results and our theoretical results, is indeed the correct value. It must be noticed that this predicted value for the ground-state totally symmetric frequency of Ag_3 is meant for a D_{3h} configuration. Any deviations in the geometry from the D_{3h} geometry will lead to larger force constants; i.e., the force constants for an isosceles trimer are expected to lie between those for the equilateral triangle and those of the linear configuration.⁴¹ Although its experimental confirmation from the ground-state emission spectra seems to be difficult, our predicted value sets a good foundation for the experimental analysis (see Part II).

While the e' frequency is not readily apparent from the spectra due to the convoluted topography of the PES near the e' vibrational cusp, its value is critical for the experimental analysis in Part II. The a'_1 mode is orthogonal to the e' subspace and is predicted to have a reasonable frequency. It is of central importance to obtain a reliable degenerate bend frequency. If we consider the central force approximation, as have others,⁴¹ the following general relations⁴⁴ come into play:

$$\nu_1^2 = 3(k_{\text{eq}}/m), \quad (40)$$

$$\nu_2^2 = 2 \cos^2(\phi/2)(k_{\text{eq}}/m), \quad (41)$$

$$\nu_3^2 = (3 - 2 \cos^2(\phi/2))(k_{\text{eq}}/m), \quad (42)$$

where m is the atomic mass of the homonuclear trimer and k_{eq} is the bond stretching force constant. In the equilateral triangle limit ($\phi=60^\circ$), $k_{\text{eq}}=m\nu_{a'_1}^2/3$, the breathing mode $\nu_{a'_1}$ and the degenerate bend mode $\nu_{e'}$ become $\nu_{a'_1}=\nu_1$ and $\nu_{e'}=\nu_2=\nu_3$, and $\nu_{a'_1}/\nu_{e'}=\sqrt{2}$. Assuming that the central force field approximation holds and that the totally symmetric frequency is 167 cm⁻¹, then one obtains an e' frequency of $\approx 120 \text{ cm}^{-1}$, a value in agreement with our theoretically calculated ground-state result.

VI. CONCLUSION

From comparisons with experiment, we conclude that the present electronic structure calculations have accurately described the \tilde{X}^2E' and \tilde{A}^2E'' states of Ag_3 . The equilibrium Ag triangle defined at the conical intersection of these states increases by a small but important amount in going from the \tilde{X}^2E' to the \tilde{A}^2E'' state. The single e' mode of Ag_3 results in a greater linear and quadratic Jahn-Teller stabilization in the \tilde{X}^2E' state than in the \tilde{A}^2E'' state.

ACKNOWLEDGMENTS

The authors are pleased to acknowledge the support of the National Science Foundation via Grant No. CHE-0511809, that of the Department of Energy, Office of Basic Energy Sciences through Grant No. ER15136, and a grant of computer time from the Ohio Supercomputer Center. The authors would also like to thank V.-A. Glezakou, A. B. McCoy, R. Tyagi, and S. Brozell for useful discussions and help with the codes.

- ¹ Y. Shen and J. J. BelBruno, *J. Chem. Phys.* **118**, 9241 (2003), and references therein.
- ² J. Yoon, K. S. Kim, and K. K. Baeck, *J. Chem. Phys.* **112**, 9335 (2000), and references therein.
- ³ E. E. Wedum, E. R. Grant, P. Y. Cheng, K. F. Willey, and M. A. Duncan, *J. Chem. Phys.* **100**, 6312 (1994), and references therein.
- ⁴ F. Wallimann, H.-M. Frey, S. Leutwyler, and M. Riley, *Z. Phys. D: At., Mol. Clusters* **40**, 30 (1997).
- ⁵ T. L. Haslett, K. A. Bosnick, S. Fedrigo, and M. Moskovits, *J. Chem. Phys.* **111**, 6456 (1999).
- ⁶ P. Y. Cheng and M. A. Duncan, *Chem. Phys. Lett.* **152**, 341 (1988).
- ⁷ P. Y. Cheng and M. A. Duncan, *Chem. Phys. Lett.* **156**, 420 (1989).
- ⁸ A. M. Ellis, E. S. J. Robles, and T. A. Miller, *Chem. Phys. Lett.* **201**, 132 (1993).
- ⁹ I. Sioutis, V. L. Stakhursky, R. M. Pitzer, and T. A. Miller, *J. Chem. Phys.* **126**, 124309 (2007), following paper.
- ¹⁰ R. L. Martin and E. R. Davidson, *Mol. Phys.* **35**, 1713 (1977).
- ¹¹ T. A. Barckholtz and T. A. Miller, *Int. Rev. Phys. Chem.* **17**, 435 (1998).
- ¹² P. García-Fernández, I. B. Bersuker, J. A. Aramburu, M. T. Barriuso, and M. Moreno, *Phys. Rev. B* **71**, 184117 (2005).
- ¹³ B. E. Applegate, T. A. Miller, and T. A. Barckholtz, *J. Chem. Phys.* **114**, 4855 (2001).
- ¹⁴ R. Meiswinkel and H. Köppel, *Chem. Phys.* **129**, 463 (1989).
- ¹⁵ U. Höper, P. Botschwina, and H. Köppel, *J. Chem. Phys.* **112**, 4132 (2000).
- ¹⁶ B. E. Applegate, A. J. Bezant, and T. A. Miller, *J. Chem. Phys.* **114**, 4869 (2001).
- ¹⁷ B. E. Applegate and T. A. Miller, *J. Chem. Phys.* **117**, 10654 (2002).
- ¹⁸ P. Pulay, *Mol. Phys.* **17**, 197 (1969).
- ¹⁹ M. C. Payne, M. P. Teter, D. C. Allan, T. A. Arias, and J. D. Joannopoulos, *Rev. Mod. Phys.* **64**, 1045 (1992).
- ²⁰ COLUMBUS programs, Release 6.0 beta 4, 2006, described at <http://www.itc.univie.ac.at/~hans/Columbus/Columbus.html>
- ²¹ See www.clarkson.edu/~pac/reps.html for complete references and a library of potentials.
- ²² B. O. Roos and P. E. M. Siegbahn, in *Methods of Electronic Structure Theory*, edited by H. F. Schaefer III (Plenum, New York, 1977), p. 277.
- ²³ R. F. Hausmann and C. F. Bender, in *Methods of Electronic Structure Theory*, edited by H. F. Schaefer III (Plenum, New York, 1977), p. 319.
- ²⁴ E. R. Davidson, *J. Comput. Phys.* **17**, 87 (1975).
- ²⁵ S. R. Langhoff and E. R. Davidson, *Int. J. Quantum Chem.* **8**, 61 (1974).
- ²⁶ E. R. Davidson and D. W. Silver, *Chem. Phys. Lett.* **52**, 403 (1977).
- ²⁷ P. E. M. Siegbahn, *Chem. Phys. Lett.* **55**, 386 (1978).
- ²⁸ P. J. Bruna, S. D. Peyerimhoff, and R. J. Buenker, *Chem. Phys. Lett.* **72**, 278 (1981).
- ²⁹ P. G. Burton, R. J. Buenker, P. J. Bruna, and S. D. Peyerimhoff, *Chem. Phys. Lett.* **95**, 379 (1983).
- ³⁰ T. H. Dunning, *J. Chem. Phys.* **90**, 1007 (1989).
- ³¹ N. M. Wallace, J. P. Blaudeau, and R. M. Pitzer, *Int. J. Quantum Chem.* **40**, 78 (1991).
- ³² P. A. Christiansen, Y. S. Lee, and K. S. Pitzer, *J. Chem. Phys.* **71**, 4445 (1979).
- ³³ ATMSCF program, original version, C. C. J. Roothaan and P. S. Bagus, *Methods Comput. Phys.* **2**, 47 (1963); ATMSCF, present version, R. M. Pitzer, *QCPE* **10**, 587 (1990). Also see R. Pitzer, *Comput. Phys. Commun.* **170**, 239 (2005).
- ³⁴ P. A. Christiansen, *J. Chem. Phys.* **112**, 10070 (2000).
- ³⁵ J. E. Sansoetti, W. C. Martin, and S. L. Young, *Handbook of Basic Atomic Spectroscopic Data (Version 1.1.2)* (National Institute of Standards and Technology, Gaithersburg, MD, 2006), available at <http://physics.nist.gov/PhysRefData/Handbook/Tables/silvertable5.htm>
- ³⁶ S. P. Walch and B. C. Laskowski, *J. Chem. Phys.* **84**, 2734 (1986).
- ³⁷ K. Balasubramanian and M. Z. Liao, *Chem. Phys.* **127**, 313 (1988).
- ³⁸ S. P. Walch, C. W. Bauschlicher, and S. R. Langhoff, *J. Chem. Phys.* **85**, 5900 (1986).
- ³⁹ K. Balasubramanian and M. Z. Liao, *J. Chem. Phys.* **86**, 5587 (1987).
- ⁴⁰ K. Balasubramanian and K. K. Das, *Chem. Phys. Lett.* **186**, 577 (1991).
- ⁴¹ J. R. Lombardi and B. Davis, *Chem. Rev. (Washington, D.C.)* **102**, 2431 (2002), and references therein.
- ⁴² G. A. Ozin and D. F. McIntosh, *J. Phys. Chem.* **90**, 5756 (1986).
- ⁴³ C. M. Brown and M. L. Ginter, *J. Mol. Spectrosc.* **69**, 25 (1978).
- ⁴⁴ G. Herzberg, *Infrared and Raman Spectra* (Van Nostrand, Princeton, 1966).
- ⁴⁵ M. N. Huda and A. K. Ray, *Eur. Phys. J. D* **22**, 217 (2003).
- ⁴⁶ V. Bonačić-Koutecký, L. Češpiva, P. Fantucci, and J. Koutecký, *J. Chem. Phys.* **98**, 7981 (1993).
- ⁴⁷ C. W. Bauschlicher, S. R. Langhoff, and H. Partridge, *J. Chem. Phys.* **91**, 2412 (1989).
- ⁴⁸ H. Partridge, C. W. Bauschlicher, and S. R. Langhoff, *Chem. Phys. Lett.* **175**, 531 (1990).
- ⁴⁹ W. Andreoni and J. L. Martins, *Surf. Sci.* **156**, 635 (1985).